A Road Ice Sensor

Amedeo Troiano, Eros Pasero and Luca Mesin

Additional information is available at the end of the chapter

http://dx.doi.org/10.5772/37749

1. Introduction

The investigation of ice formation found important applications in many different fields. For instance, the accretion of ice is a common occurrence on the aircraft, due to the high velocity and humidity, and low temperature at upper air. The detection of ice formation on aircrafts is a critical issue since not only the aerodynamics change, but there is also the possibility of ice liberation from the aircraft during the flight, and falling ice could strike and possibly damage the engine [23]. Another applications of the investigation of ice formation are on the seas, in order to prevent iceberg formation and possible accident due to the crash with boats [39]. An adequate assessment of the environmental conditions of road surfaces may significantly contribute to enhance traffic safety, since corresponding decision made by administrators should be based on this information [18]. An important application of the investigation of ice formation is on the runway of airports, in order to improve safety during take off and landing of the aircrafts. Moreover, a correct estimation of the environmental condition of road and runway surfaces can be useful to reduce costs due to de-icing systems and ice control [27]. Finally, an indication of the environmental condition of the pavements could be adopted on the walkways, to prevent people falls.

2. State of the art

The problem of ice detection is not a new one: over the time, several solutions have been proposed depending on the application [9]. The proposed solutions can be divided into two families: detection of ice based on optical methods and using physical sensors.

Optical methods are indirect techniques that detect icy conditions applying image-processing algorithms to the images acquired by different systems. Wide-area ice detection can be obtained processing images by weather satellites [17, 26, 37], which are used to monitor the climate of the Earth. Weather satellites can be either polar orbiting, seeing the same swath of the Earth, or geostationary, hovering over the same spot on Earth by orbiting over the equator while moving at the speed of the Earth's rotation. One of the most used optical method is based on Time-Domain Reflectometry (TDR) technique [4, 32]. TDR is

a measurement technique commonly used to determine characteristics of electrical lines by observing reflected waveforms. The time-domain reflectometry technique can also be used for detection of ice and water on the road, based on the principle that the propagation velocity of an electromagnetic wave in a transmission line depends on the relative permittivity of the material; and the relative permittivity, in turn, depends on the water or ice content of the medium. Ice detection can be also obtained using microwave systems [6]. A MicroWave Radiometer (MWR) is a system that measures energy emitted at sub-millimetre to centimetre wavelengths (at frequencies of 1-1000GHz), known as microwaves. Studying the physical processes associated with the energy emission at these wavelengths, it is possible to estimate a variety of surface and atmospheric parameters, including air and sea surface temperature, salinity of sea ice, precipitations, and sea ice. River and sea ice can be detected applying specific algorithms to the data collected by acoustic Doppler current meters [11]. These instruments are designed for monitoring water level, velocity, and flow of rivers and seas. Since the velocity distribution of water changes significantly when ice is present, specific algorithms can be developed to determine the presence of ice in rivers or seas. Ocean ice can be detected processing the images obtained by MODerate resolution Imaging Spectroradiometer (MODIS) [22, 39]. MODISs are instruments launched into Earth orbit by NASA in 1999 on board of satellites. MODIS captures images of the entire Earth using spectral bands ranging in wavelength from 0.4μm to 14.4μm, at different spatial resolutions. The last optical method used for the detection of ice is based on ultrasonic waveguides [3, 7, 16], that are structures which guide waves, such as electromagnetic or sound. Ultrasonic guided waves can recognizes water or ice since the amplitude of the A0 mode Lamb wave is influenced by water loading and ice formation on the surface of the aluminum plate of the waveguide.

In order to detect ice directly, physical sensors are used. An ice detection system based on a physical sensor can be obtained using micro-fabricated diaphragms as sensing elements [29]. Accumulation of ice on a diaphragm leads to an increase in its effective stiffness. The sensor is composed by a diaphragm, which is the sensing element and is electrically isolated, and an electrode. When a voltage is applied between the diaphragm and the electrode, an attractive electrostatic force will cause the diaphragm to deform toward the electrode, increasing the capacitance between the electrode and the diaphragm. For a given actuation voltage, it was shown that an ice-covered diaphragm exhibits a smaller deflection than a corresponding ice-free diaphragm. Another kind of ice detection system designed for aircrafts is obtained using fiber optics [12, 13, 20, 21]. When there is no ice accretion on the probe surface, the light from the emitter propagates through the source fiber bundle into the air, and no signal can be detected by the destination fiber bundle. When there is ice accreting on the probe, light entering the volume of ice is in part transmitted and in part reflected into the destination fiber bundle, which couples with the detector that determines the thickness of ice depending on the light intensity distribution. Physical sensor for ice detection system can also be based on resonant piezoelectrics [30]. Resonant structures are commonly used in sensor systems due to their high sensitivities to small variations in applied loads. Ice detection systems based on resonant sensors are based on the principle that accretion of ice on a cylindrical probe leads to a decrease in the measured resonant frequency, due to the increase in effective mass of the resonator. In such mass-loaded resonant ice detection sensor, variations in probe design are usually restricted to favor ice accretion and minimize resonant frequency shifts due to accumulation of water and other fluids.

3. The ice detection system

The previously described methods do not fit the requirements for a direct detection of ice in the road or in the runway surfaces. For example, optical methods cannot be used for this application because they are indirect techniques. Moreover, resonant probes are too power consuming and optical fibers are too expensive for the development of this sensor. Since the sensor should be embedded in the road or in the runway, it has to resist on the pressure of trucks or airplanes, or also possible chemical substances present on the road or on the runway, so diaphragms cannot be used for the presented application. For these reasons, an innovative sensor for water and ice detection was designed.

The ice detection system consists of a relative permittivity measurement [25, 33–36]. In general, permittivity is defined as a measure of how an electric field affects and is affected by a dielectric medium, and is determined by the ability of a material to polarize in response to the field, and thereby to reduce the total electric field inside the material. The relative permittivity (also called dielectric constant) is the ratio of the amount of stored electrical energy when a potential is applied, relative to the permittivity of the vacuum. The relative permittivity depends on temperature and measurement frequency. The relation between the relative permittivities of water and ice, and the temperature and measurement frequency, is shown in Figure 1 [5, 31, 38] (note the different scales of the frequency axes). It can be seen that the relative permittivity of ice at approximately -1°C is substantially constant within a range from DC to about 1kHz, and decreases in the range of approximately 2kHz to several hundred kHz. On the other hand, the relative permittivity of water at approximately 1°C is substantially constant up to approximately 10^9Hz and decreases within the range from 10^9Hz to 10^{10}Hz. The relative permittivity of air can be assumed to be equal to 1 and constant for each frequency and temperature. Therefore, at low frequencies the relative permittivities of water and ice are similar, while the relative permittivity of air is different from the others. Instead, at high frequencies the relative permittivities of air and ice are similar, while the relative permittivity of water is different from the others [25, 33–36]. So, estimating the relative permittivity, it is not possible to distinguish reliably water and ice at low frequencies (lower than 1kHz), but only air can be identified; on the other hand, ice and air cannot be distinguished at high frequencies (between 10kHz and 1GHz), but it is possible to identify only the presence of water. Thus, for an exact classification of the material placed over the sensor, distinguishing among ice, water, or air, it is necessary to estimate the relative permittivity of the material on the surface of the sensor at two frequencies (low and high frequency).

The relative permittivity can be sensed by a capacitance measurement. In general, the capacitance value of an electrode assembly depends on the geometrical configuration and dimensions of the surfaces of the electrodes, and on the permittivity and thickness of the material placed between the electrodes. The device consists in a multi-frequency capacitance measurement. As low measurement frequency 200Hz was considered; while 20MHz was chosen as high measurement frequency. The sensor includes a pair of concentric conductive electrodes (with geometry and dimensions shown in Figure 2). Such electrode geometry was chosen since the capacitance measurement is invariant to the rotations of the electrode assembly and to the position of raindrops or pieces of ice with respect to the electrodes. The pair of concentric ring conductive electrodes, which are the sensing device, was directly implemented on a PCB, as showed in Figure 2. The external maximum ring dimension was imposed by the box which includes the sensor, while the external minimum ring and internal circle dimensions were choosen in order to explore a largest area between the two electrodes,

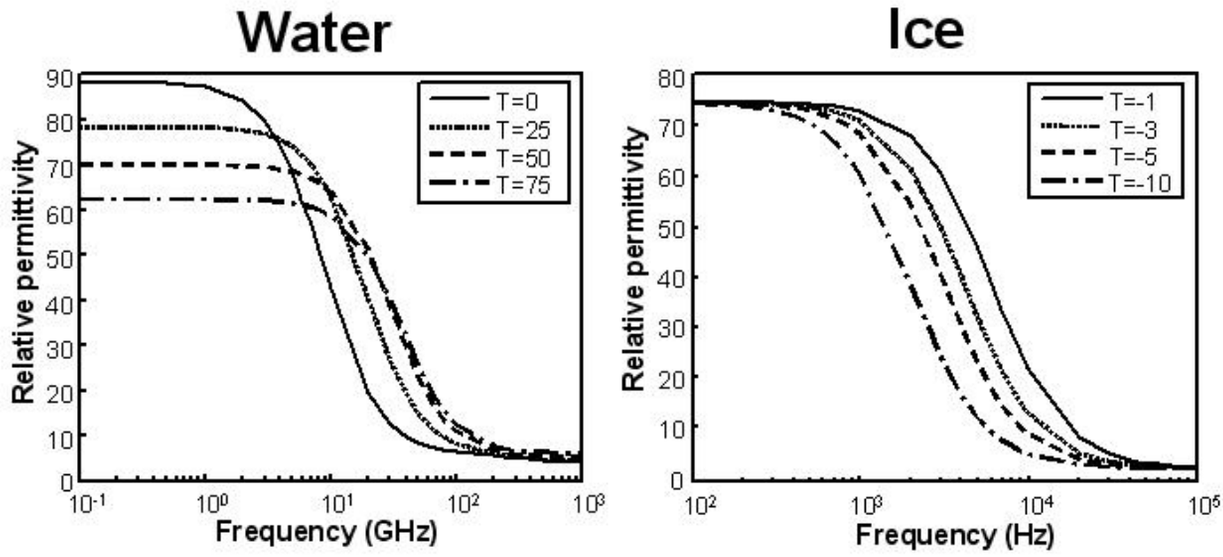

Figure 1. Representation of the relative permittivity of water and ice at different frequencies and temperatures.

but still large enough to get a measurable value of capacitance. The capacitance value of the pair of concentric ring conductive electrodes was measured using a high resolution RCL meter (Fluke - PM 6306). The capacitance value was in the order of 0.3pF.

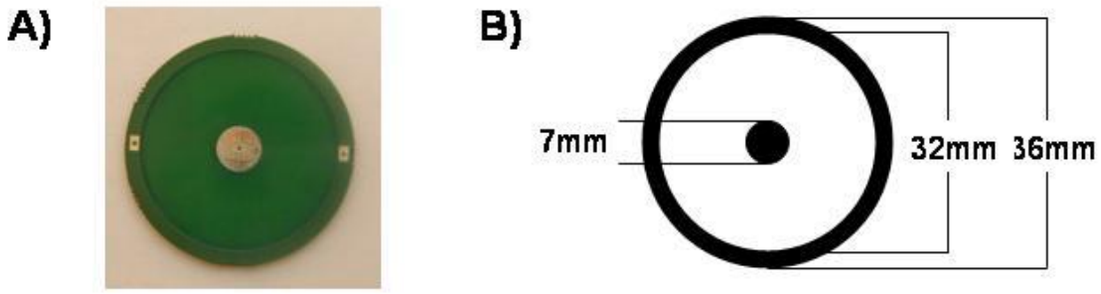

Figure 2. Representation of the pair of concentric ring conductive electrodes. A) Top view of the electrode assembly. B) Geometry of the electrode assembly.

The sensor electrodes of the ice detector are directly connected to a capacitance measurement system, which is a transfer charge circuit. In general, the transfer charge circuit includes a sensing capacitor, a frequency generator, and a charge detector. The schematic layout of the capacitive measurement circuit is shown in Figure 3. The sensing capacitor is obtained by the pair of concentric conductive electrodes and the material placed over the electrodes, and it is indicated in the Figure as C_X. The frequency generator is obtained by a reference voltage source V_R and a controllable switch S_1 to provide different frequencies. In the basic measurement circuit, the charge detector comprises only a reference capacitance C_S that is connected to C_X by closing the switch S_2. Note that S_2 opens when S_1 is closed, and viceversa. The charge Q_X stored in the electrode assembly is:

$$Q_X = C_X \cdot V_R \tag{1}$$

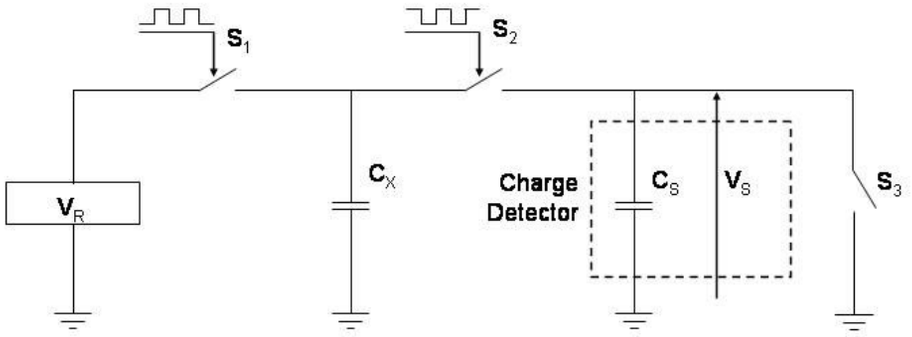

Figure 3. Schematic layout of the transfer charge circuit

When the switch S_2 is closed, the charge stored in the electrode assembly is transferred to the detection capacitance:

$$Q_X = (C_S + C_X) \cdot V_S \tag{2}$$

Since the value of the sensor electrode is several orders of magnitude lower than C_S, nearly all charge stored in C_X is transferred to the detection capacitance:

$$Q_X = C_X \cdot V_R = C_S \cdot V_S \tag{3}$$

and therefore, measuring the voltage level V_S reached by the detection capacitance, the capacitor value of the electrode assembly can be computed as:

$$C_X = C_S \cdot \frac{V_S}{V_R} \tag{4}$$

In order to increase accuracy in measuring the very small value of the capacitance C_X, the sensor was charged n times and its charge was transferred n times to the reference capacitor before taking a measurement of V_S. Therefore the value of the capacitance of the electrode assembly is given by:

$$C_X = \frac{C_S}{n} \cdot \frac{V_S}{V_R} \tag{5}$$

At the end of the measurement process, C_S is discharged by closing the switch S_3. In the currently available ice sensor, the reference voltage V_R was equal to 3V (tolerance of 0.2%), the value of the reference capacitance C_S was equal to 2.2nF (tolerance equal to 1%), and the number of times in which the reference capacitor was charged before taking a measurement (n) was 50. The voltage V_S was first amplified by a factor 150 by an analog circuit and then sampled by the analog to digital converter (10 bit resolution) of a microcontroller (8051 microcontroller from Silicon Laboratories Inc). The microcontroller is also used to drive the switches S_1, S_2, and S_3. These operations are performed for both measurement frequency in sequence, low and high frequencies, using a sampling frequency of 0.2Hz. The transfer charge circuit is implemented on a PCB using commercially available low power and low cost components. The PCBs of the electrodes arrangement and of the transfer charge circuit are directly connected together.

As it stated above, the value of capacitance of the electrode assembly (without water or ice placed over it) is about 0.3pF. However, parasitic capacitances of wires and electronic circuits are, in general, on the order of several pF. Therefore, the value of parasitic capacitances is bigger than that of the unknown capacitance, and consequently it is not possible to estimate

the capacitance of the electrode assembly using the previously described circuit. In order to prevent error in the data due to parasitic capacitances, a differential capacitance measurement circuit was used. Parasitic capacitances are first estimated in a preliminary calibration phase, performed in laboratory, measuring the capacitance of the sensor without placing water or ice over the electrode assembly, and the measured value is stored in the flash memory of the microcontroller. This value results from the combination of the capacitance of the dry electrode assembly and the parasitic capacitances. Then, during the measurement, the obtained value of V_S is subtracted by the calibration value in order to remove the contribution of parasitic capacitances (also the value of the dry electrode assembly is removed). The calibration value stored in the flash memory of the microcontroller, which is subtracted to the measured value, is obtained by the digital to analog converter (10 bit resolution) of the microcontroller. A schematic layout of the differential capacitance measurement circuit is shown in Figure 4.

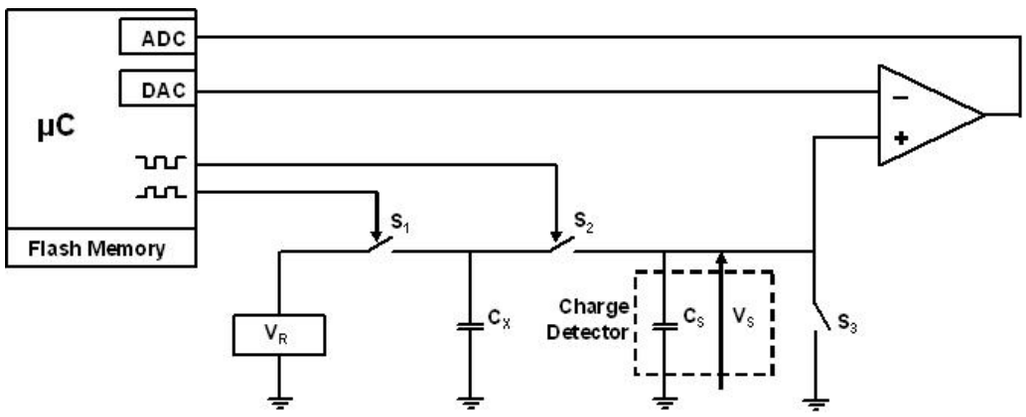

Figure 4. Schematic layout of the differential capacitance measurement circuit.

The device also comprises a temperature sensor, to account for the variation of the relative permittivity with temperature. The temperature obtained by the sensor is sampled by the analog to digital converter (10 bit resolution) of the microcontroller, using a sampling frequency of 0.2Hz.

The ice detection system arrangement (circuit and electrode assembly) was included in a metallic box filled with resin, which protects the circuitry from infiltration of water or chemical agents. The only exposed parts are the Arnite covering the sensor (on the top) and the connector for the power supply and the RS 485 communication protocol (on the bottom). Arnite (Polyethylene Terephthalate) was chosen for protection purposes since its relative permittivity is nearly constant within the range of temperatures and measurement frequencies in which the sensor is used. Moreover, it has a high value of hardness to steel ball (180 $\frac{N}{mm^2}$) and resistance to traction (255 $\frac{N}{mm^2}$). A layer 3 mm thick of Arnite was mounted over the electrode assembly. The final prototype of the ice detection system is shown in Figure 5.

4. Mathematical model of the sensor

A mathematical model of the sensor was designed. The sensor was described using a multilayer electrostatic model [15]. Indeed, at the maximum measurement frequency the wave length of the electromagnetic field is more than two orders of magnitude greater than the dimensions of the sensor. Three layers were included: dielectric (the Arnite protecting the

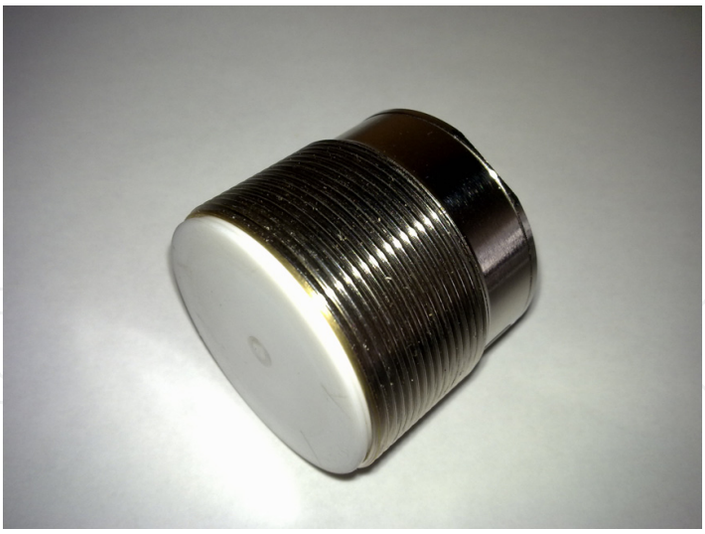

Figure 5. Picture of the final prototype of the ice detection system.

sensor) covering the electrodes (z_1), air or water or ice placed over the sensor (z_2), and air (z_3), as showed in Figure 6 (z_i indicates the thickness of each layer). Each layer was assumed to be homogeneous, isotropic, of constant thickness, and with a constant value of relative permittivity (ε_i). These three layers were positioned over the concentric circular electrode arrangement constituted by a circular electrode of radius 3.5mm (r_0) and a ring electrode with external radius of 18mm (r_{EXT}) and an internal one of 16mm (r_{INT}).

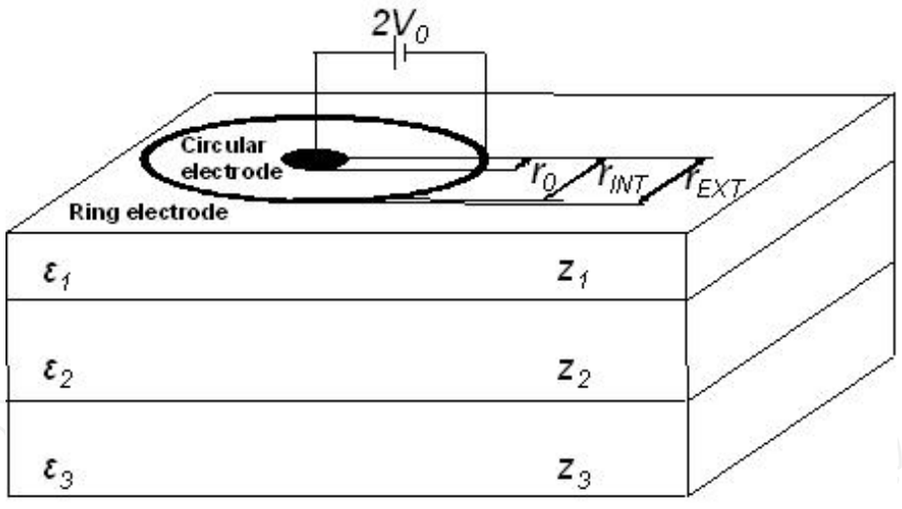

Figure 6. Representation of the three layers model of the sensor.

For the first layer, the Arnite, a constant value of relative permittivity ε_1 was assumed, equal to 3.5. For the second layer, the relative permittivity of water, ice, or air was modelled. The relative permittivity of water ε_2 was modelled as [24]:

$$\varepsilon_2 = \varepsilon_\infty + \frac{\varepsilon_s - \varepsilon_i}{1 + j\frac{f}{f_1}} + \frac{\varepsilon_i - \varepsilon_\infty}{1 + j\frac{f}{f_2}} \tag{6}$$

where all parameters (static permittivity ε_s, high frequency permittivity ε_∞, intermediate frequency permittivity ε_i, and relaxation frequencies f_1 and f_2) are functions of temperature.

The relative permittivity of ice (again indicated with ε_2) was modelled as a Debye model [8]:

$$\varepsilon_2 = \varepsilon_\infty + \frac{\varepsilon_s - \varepsilon_\infty}{1 + j2\pi\tau f} \tag{7}$$

in which the static permittivity ε_s was 75, the high frequency permittivity ε_∞ was 3.2, and the relaxation time τ was dependent on temperature, assuming a linear variation between the values $1.4 \cdot 10^{-4}$ at -20°C and $2.5 \cdot 10^{-5}$ at 0°C [28]. The relative permittivity ε_3 of the third layer, the air, was assumed constant and equal to 1.

The mathematical model of the sensor is an electrostatic equation for dielectrics. Gauss's law for dielectrics [15], is considered:

$$-\nabla \cdot (\varepsilon \nabla \phi) = 0 \tag{8}$$

where ϕ is the potential (V) and ε the relative permittivity (F/m). Since the mathematical model is constituted by three layers, the electrostatic equation for dielectrics was studied in different sub-domains in which Laplace equation $\Delta\phi = 0$ was solved (with $\Delta = \nabla^2$). Each sub-domain indicates a layer. Such sub-domains were coupled by the interface conditions between two layers requiring that the potential and the dielectric displacement $\vec{D} = \varepsilon\nabla\phi$ were continuous crossing the interface.

As the electrodes are circular (see Figure 6), the problem was considered symmetrical in cylindrical coordinates (ρ, θ, z). A mixed boundary value problem was studied, imposing opposite value of potential (indicated as V_0 in Figure 6) on the two electrodes and vanishing dielectric displacement on the other part of the boundary. Due to the cylindrical symmetry of the problem, the potential does not depend on the angle θ, but only on the radius ρ and on the depth within the layers z. The problem can be stated as follows:

$$\begin{cases} \Delta\phi_1 = \frac{\partial^2\phi_1}{\partial\rho^2} + \frac{1}{\rho}\frac{\partial\phi_1}{\partial\rho} + \frac{\partial^2\phi_1}{\partial z^2} = 0 & \rho > 0,\ 0 < z < z_1 \\ \Delta\phi_2 = \frac{\partial^2\phi_2}{\partial\rho^2} + \frac{1}{\rho}\frac{\partial\phi_2}{\partial\rho} + \frac{\partial^2\phi_2}{\partial z^2} = 0 & \rho > 0,\ z_1 < z < z_1 + z_2 \\ \Delta\phi_3 = \frac{\partial^2\phi_3}{\partial\rho^2} + \frac{1}{\rho}\frac{\partial\phi_3}{\partial\rho} + \frac{\partial^2\phi_3}{\partial z^2} = 0 & \rho > 0,\ z_1 + z_2 < z < z_1 + z_2 + z_3 \\ \phi_1 = \phi_2 & \rho > 0,\ z = z_1 \\ \phi_2 = \phi_3 & \rho > 0,\ z = z_1 + z_2 \\ \varepsilon_1\frac{\partial\phi_1}{\partial z} = \varepsilon_2\frac{\partial\phi_2}{\partial z} & \rho > 0,\ z = z_1 \\ \varepsilon_2\frac{\partial\phi_2}{\partial z} = \varepsilon_3\frac{\partial\phi_3}{\partial z} & \rho > 0,\ z = z_1 + z_2 \\ \phi = V_0 e^{j2\pi ft} & \rho \le \rho_0,\ z = 0 \\ \phi = -V_0 e^{j2\pi ft} & \rho_{INT} \le \rho \le \rho_{EXT},\ z = 0 \\ \frac{\partial\phi}{\partial\rho} = 0 & \rho = 0 \\ \frac{\partial\phi}{\partial z} = 0 & \rho_0 < \rho < \rho_{INT} \cup \rho > \rho_{EXT},\ z = 0 \\ \frac{\partial\phi}{\partial z} = 0 & z = z_1 + z_2 + z_3 \end{cases} \tag{9}$$

where ρ_0 is the radius of the internal electrode, ρ_{INT} and ρ_{EXT} are the internal and external radiuses defining the ring shape electrode, and z_1, z_2 and z_3 are the thicknesses of the layers. The estimated capacitance is a monotonic increasing function of the thickness of the third layer (air), but saturates within a few simulated mm of air; thus, the simulated thickness of air was chosen to be 25mm, assuring that the capacitance curve saturates.

In order to solve the mathematical problem, the domain should be limited. The domain was limited imposing a maximum radius of 30mm where homogeneous Neumann boundary conditions $\frac{\partial \phi}{\partial \rho} = 0$ were assumed. The mathematical problem was solved using the finite difference method, which is a numerical method for approximating the solutions of differential equations using finite difference approximation of derivatives [19]. A non-uniform discretization of the domain was used, with increasing resolution close to the electrodes and to the interfaces. Specifically, the sampling step of the radius $\Delta\rho$ was 1% of the maximum radius (30mm) close to the electrodes and 3% of the maximum radius otherwise. The discretization step of the depth variable Δz was 1% of the sum of the thickness of the three layers $z_1 + z_2 + z_3$ close to the electrode surface $z = 0$ and to the interfaces $z = z_1$ and $z = z_2$, and 3% of the before indicated sum otherwise.

First and second order derivatives were discretized, using the finite difference method, with a second order approximation, both within the domain and on the boundary:

$$\begin{aligned}
&\left.\frac{\partial u}{\partial x}\right|_{x_0} \cong au(x_0) + bu(x_0 + h_1) + cu(x_0 + h_2);\\
&\text{where a} = -\tfrac{h_1+h_2}{h_1 h_2},\ \text{b} = -\tfrac{h_2}{h_1(h_1-h_2)},\ \text{c} = \tfrac{h_1}{h_2(h_1-h_2)}\\
&\left.\frac{\partial^2 u}{\partial x^2}\right|_{x_0} \cong au(x_0) + bu(x_0 + h_1) + cu(x_0 + h_2);\\
&\text{where a} = \tfrac{2}{h_1 h_2},\ \text{b} = \tfrac{2}{h_1(h_1-h_2)},\ \text{c} = -\tfrac{2}{h_2(h_1-h_2)}
\end{aligned} \tag{10}$$

where h_1 and h_2 have the same sign when the considered point x_0 is on the boundary and different signs when x_0 is within the domain. A linear system of algebraic equations was obtained after discretization. The potential was estimated resolving such a system using Gauss elimination method. Given the potential, the charge q over the internal electrode (which is the same except for the sign as that over the external ring electrode) was estimated, using the integral form of Gauss's law [15], as:

$$q = \Re\left[\int_{\rho \le \rho_0,\, z=0} \vec{D} \cdot \hat{n} dS\right] = 2\pi\varepsilon_1 \int_0^{\rho_0} r \frac{\partial \Re[\phi]}{\partial r} dr \tag{11}$$

Finally, the capacitance value was obtained as [15]:

$$C = \frac{q}{2V_0} \tag{12}$$

The mathematical model of the sensor was validated using both analytical and experimental data [36]. Validation based on analytical data was obtained changing the boundary conditions of the model, allowing the simulation of a capacitor with parallel planar plates with a layer of dielectric covering the plates. The relative error between the analytical and simulated solutions was lower than 1.5%. Validation based on experimental data was performed simulating the dry sensor, in which a capacitance value of about 0.3pF was obtained. This is the capacitance value of the dry electrode arrangement, which was measured using a high resolution RCL meter (Fluke - PM 6306), indicating a capacitance value of about 0.3pF. Moreover, simulated and experimental values of capacitance were compared for different temperatures and frequencies, and placing water or ice over the sensor. Results shown a relative error between the experimental and simulated solutions lower than 2%.

5. Results

5.1. Laboratory results

The reliability of the estimates provided by the sensor was investigated during laboratory experiments. Laboratory tests were performed applying the same environmental conditions to more sensors and evaluating the dispersion of the time instants in which phase changes of water were detected. Nine sensors were placed at the same time in a climatic chamber (Angelantoni - Challenge 250; temperature range for climatic test from -40°C to +180°C). At the beginning of the experiment, the climatic chamber was set to ambient conditions, with a temperature of 25°C and humidity of 50%, for approximately 10 minutes in order to adjust the parameters of the sensor. Then, 1 mm of tap water was placed over each sensor. Sensors were left in ambient conditions for 10 minutes. Then, the climatic chamber was arranged to reach -20°C with a temperature gradient of -1°C per minute. During this period, water placed over sensors frozes. The climatic chamber kept the temperature of -20°C for approximately 10 minutes and then it was arranged to reach 25°C with a temperature gradient of 1°C per minute. During this period, the ice formed over the sensors melts. The climatic chamber kept the temperature of 25°C for approximately 10 minutes. Then each sensor was dried. Data were acquired for additional 10 minutes, with a temperature of 25°C and humidity of 50%. The experiment was repeated in three different days, in order to investigate the repeatability of the capacitance values and the reliability of the estimates provided by the algorithm.

During the experiments, values of capacitance at different measurement frequencies (200Hz, 500Hz, and 20MHz) were continuously acquired. In Figure 7 the data acquired and processed from the sensor eight during the first experiment are shown. In detail, Figure 7A shows the capacitance values (raw data) at different measurement frequencies. Variations of the values of capacitance in different states of the sensors are visible. During the dry state, values of capacitance (at both low, medium, and high frequencies) were close to zero, due to the calibration procedure. During the wet state, the values of capacitance at high, medium, and low frequency were close to 0.3pF, so there is no distinction between different measurement frequencies (since the relative permittivity of water is constant at both low, medium, and high frequencies). However, during the icy state, the values of capacitance at high frequency are close to 0.15pF while at medium and low frequency are close to 0.3pF (since the relative permittivity of ice is different at both low and medium frequencies with respect to that at high frequency), so the value of capacitance can be easily distincted for different measurement frequencies. Moreover, there are no differences between values of capacitance obtained for low and medium frequencies. Low pass (cut-off frequency of 0.002Hz, 100^{th} order causal FIR filter) filtered values of capacitance are shown in Figure 7B. It can be seen that high frequency variations and instrumentation noise are not present in the filtered capacitance values.

First-order derivative of the filtered values of capacitance are shown in Figure 7C (below). Peaks are visible near the variation of the state of the sensor. During the state transition from dry to wet, a concurrent positive jump at high and low (and medium) measurement frequencies is visible. A negative jump at high measurement frequency and no jump at low (and medium) measurement frequency indicate the state transition from wet to icy. During the state transition from icy to wet, a positive jump at high measurement frequency and no jump at low (and medium) measurement frequency are visible. Finally, a concurrent negative jump at high and low (and medium) measurement frequencies indicates the state transition from wet to dry. In order to discriminate between different states of the sensor surface (dry, wet, or icy), an algorithm was implemented based on the jumps on the first-order derivative

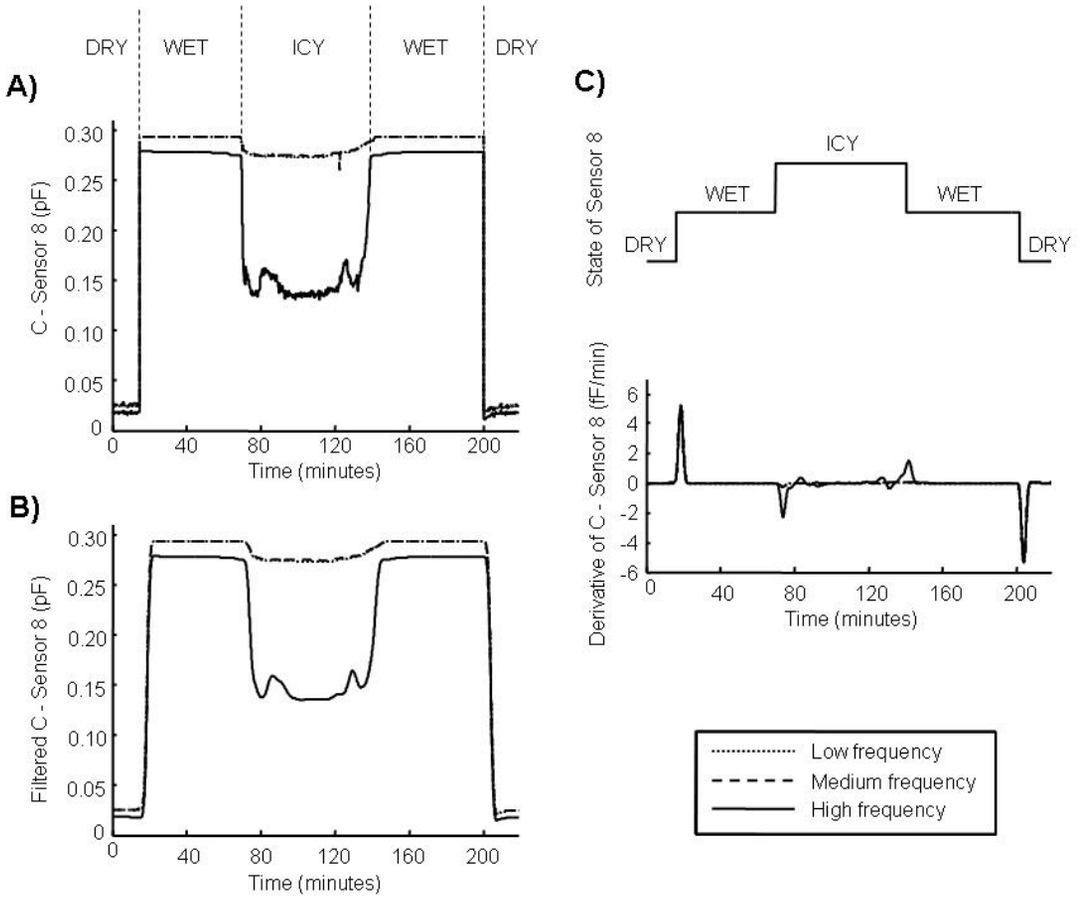

Figure 7. Signal processing algorithm applied to experimental data. A) Capacitance's values (raw data) obtained for the sensor eigth during the first experiment at different measurement frequencies. B) Low pass filtered values of capacitance obtained from the raw data. C) States of the sensor revealed by the algorithm (above). First-order derivative of capacitance values obtained from the low pass filtered data (below).

of the values of capacitance estimated at the low and high measurement frequencies. A jump was considered significant if the first-order derivative of the capacitance was higher than a threshold value estimated during the calibration. States of the sensor revealed by the algorithm are shown in Figure 7C (above). The estimated states agreed with the observed state of the sensor, showed in Figure 7A.

The reliability of the estimates provided by the sensor was investigated during laboratory experiments. Nine ice sensors were placed at the same time in a climatic chamber and the experiment descript above was performed, and the dispersion of the time instants in which phase changes of water were detected. Capacitance values (raw data) at two frequencies (low and high measurement frequencies) obtained for each sensor during the first experiment are shown in Figure 8A (medium measurement frequency is not reported since its capacitance values are very similar to that obtained at low measurement frequency). There are no difference between the capacitance values obtained at low and high measurement frequencies during the dry and wet states for different sensors; however, during the icy state there are a clear distinction. The capacitance values obtained in the icy state for different sensors are not the same due to manufacturing tolerances and low precision in controlling the thickness of water placed over the sensor. In Figure 8B, the internal temperature of the climatic chamber

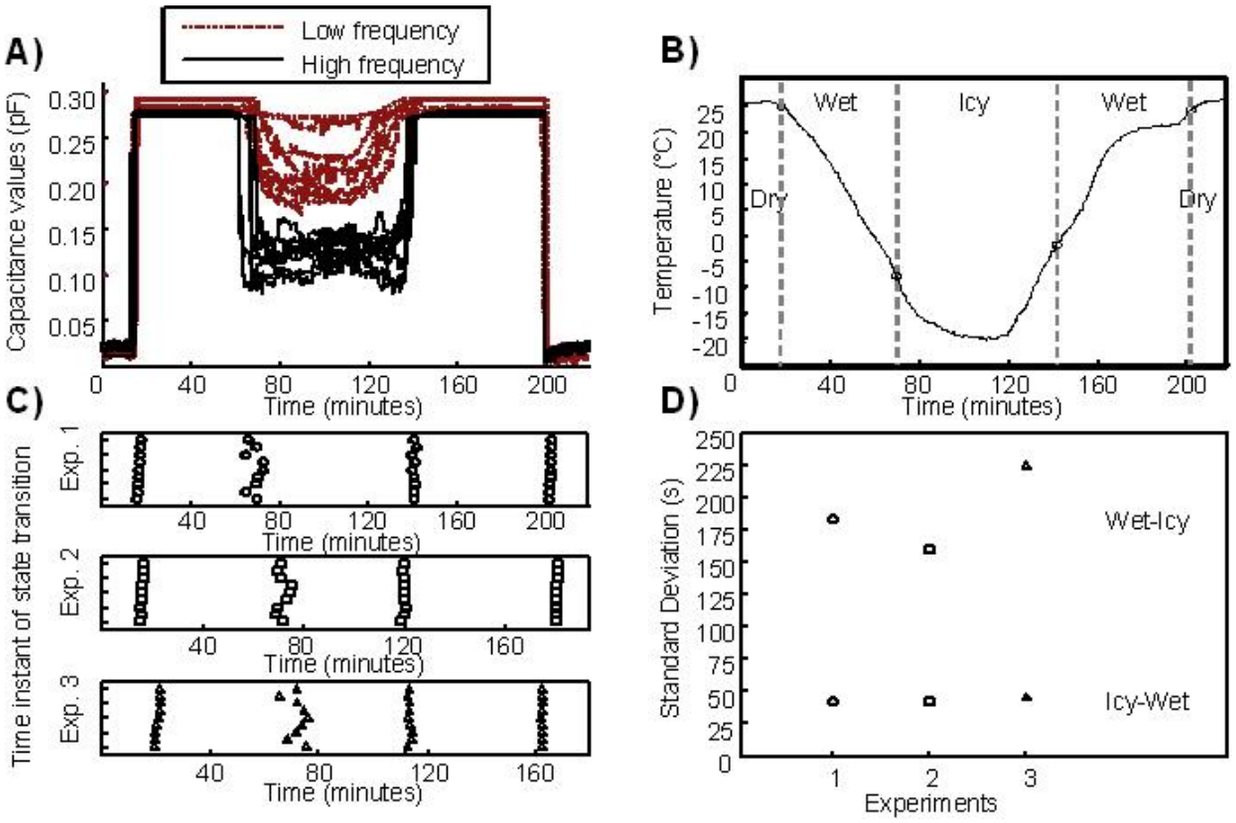

Figure 8. Statistical analysis of laboratory data. A) Values of capacitance (raw data) obtained for each sensor during the experiment. B) Internal temperature of the climatic chamber during the experiment. C) Time instants of state transitions estimated for each sensor during three experiments. D) Standard deviations of time instants of state transitions wet-icy and icy-wet estimated for each sensor during three experiments.

during the experiment is shown, and the state condition detected by one of the nine sensor is also indicated. The wet-icy transition is identified at about -7°C, whereas the icy-wet transition is identified when the internal temperature is about 0°C. So, the wet-icy transition was detected at lower temperatures than the icy-wet transition, probably due to the higher value of specific heat for water (about 4000 J kg^{-1} K^{-1}) with respect to ice (about 2000 J kg^{-1} K^{-1}), which determines a higher time to cool water than that needed to warm ice, keeping constant the magnitude of the temperature gradients imposed by the climatic chamber.

In order to study the repeatability of the estimates provided by the sensor, three experiments were performed. Time instants of state transitions estimated for each sensor during the three experiments are shown in Figure 8C. Differences of the estimated times of transition were in the order of a few minutes, which is related to the spatial heterogeneity of the icing and melting processes. The standard deviations of the time instants of the state transitions wet-icy and icy-wet estimated for each sensor are shown in Figure 8D. The time instants of the state transitions dry-wet and wet-dry were not considered, since the sensor were wetting and drying by the user. The standard deviation obtained for three experiments for the state transition wet-icy was larger than that obtained for the state transition icy-wet. Indeed, water started freezing from the surface proceeding downward, so a small difference in the thickness of the layer of water could determine a spread of the delays of different sensors in the identification of the presence of ice. On the other hand, the melting process started at

the sensor surface (probably due to low energy dispersions from the device). Moreover, there is no relevant difference between the standard deviation values obtained in the same state transitions for three experiments.

5.2. Simulation results

The reliability of the capacitance estimates provided by the mathematical model of the sensor was investigated during a simulation tests, applying the same simulated conditions of the laboratory experiment. At the beginning of the test, the sensor has a simulated temperature of 25°C in the state dry. After 18 samples, the simulated state of the sensor became wet, and the temperature decrease up to -20°C with a temperature gradient of -1°C per sample. During this period, at 0°C, the water over the sensor frozes. When the simulated temperature reached -20°C, it increased up to 25°C with a temperature gradient of 1°C per sample. During this period, at 0°C, ice melts. When the simulated temperature reached 25°C, the state of the sensor became dry. The simulation test ends after 18 more samples.

Simulated capacitance values obtained using the mathematical model at different measurement frequencies and simulated temperature values are shown in Figure 9A. During the simulated dry and wet states of the sensor, the values of capacitance at high, medium, and low frequencies were close to 0.3pF and 0.6pF, respectively. During the simulated icy state of the sensor, the values of capacitance at high frequency were close to 0.45pF whereas at medium and low frequencies were close to 0.6pF. Thus, there were difference on the simulated capacitance values at different frequencies, reflecting the variation of the relative permittivity of ice with frequency. The obtained simulated capacitance values are very similar to those obtained during the laboratory test (see Figure 7), subtracting the calibration value, which is about 0.3pF. This demonstrates the validity of the mathematical model. Low pass filtered values of simulated capacitance are shown in Figure 9B. First-order derivative of the simulated filtered values of capacitance are shown in Figure 9C (below). Peaks are clearly visible near the variation of the state of the sensor. States of the sensor revealed by the algorithm, using simulated data, are shown in Figure 9C (above). The estimated states agreed with the simulated state of the sensor, showed in Figure 9A.

The mathematical model are used to characterize the sensor in different situations. Two simulation tests were performed, the first one oriented to the effect of the thickness of water or ice placed over the sensor, the second one oriented to the study of the capacitance values at different measuring frequencies when water or ice was placed over the sensor.

The values of capacitance obtained using the mathematical model at different thicknesses of water, from 0 (dry sensor) to 10mm, are shown in Figure 10A (temperature of 25°CC and measurement frequency of 20MHz, but equivalent results are obtained for lower frequencies). Capacitance values rose slightly increasing the thickness of water over the sensor. Simulated values of capacitance for different thicknesses of ice are also shown in Figure 10A (temperature of -10°CC and measurement frequency of 200Hz and 20MHz). Also increasing the thickness of ice formed over the sensor the capacitance values rise. Simulated values of capacitance obtained for different measurement frequencies of water and ice are shown in Figure 10B (thickness of 1mm, and temperature of 25°CC for water and -10°CC for ice). Increasing the measurement frequency, the values of capacitance decreased, following the same trend of the relative permittivity.

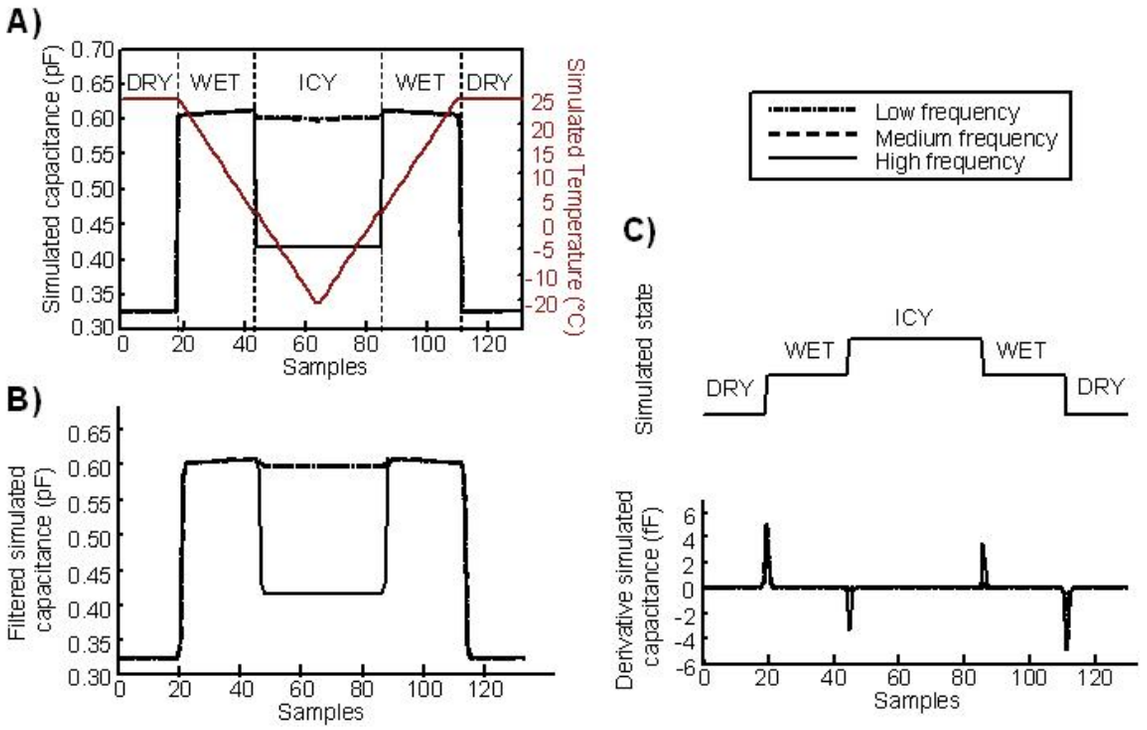

Figure 9. Signal processing algorithm applied to simulation data. A) Simulated capacitance values obtained during the simulation test at different measurement frequencies. B) Low pass filtered values of the simulated capacitance. C) States of the sensor revealed by the algorithm (above). First-order derivative of the low pass filtered simulated capacitance values (below).

5.3. Comparison of ice detection over the sensor and on the surface of a road

In order to detect ice formation on the surface of a road or a runway, embedding the sensors directly on the pavements is preferable. However, the surface of the sensor is flat and very different from that of the road, which is a rough surface due to the bitumen. Moreover, the sensor blocks percolation of water, which is very important in determining the road surface conditions. Thus, the icing and melting processes on the sensor and on the surface of a road may have a deviation, which is difficult to predict. In order to address this issue, some sensors were covered by bitumen [35, 36]. The bituminization process was performed in laboratory, and the experiment descript above was performed using bituminized sensors. The bitumen do not affect the measurement since the values obtained by bituminized sensors are the same of that obtained by sensors without bitumen. The reason is that bitumen has a very small value of relative permittivity ($\varepsilon_r = 3$, close to the value of relative permittivity of the Arnite) and this value does not change with the measurement frequencies [35, 36].

Nevertheless, the icing process over a bituminized sensor may be different from that of a road even if the two surfaces are the same, since percolation under them is different. For this reason the indications provided by the sensor were compared with the ice formation and melting over a road model identified by direct inspection. The road model was obtained using a road core with diameter of 30 cm and thickness of 20 cm. It is constituted by three layers, with asphalt and concrete with different granularity, allowing a good distribution of loads and a proper drain and filtration. In order to compare the indication of presence of ice provided by the sensor with the ice formation and melting over a road, experimental tests were performed applying the same environmental conditions to three sensors and to

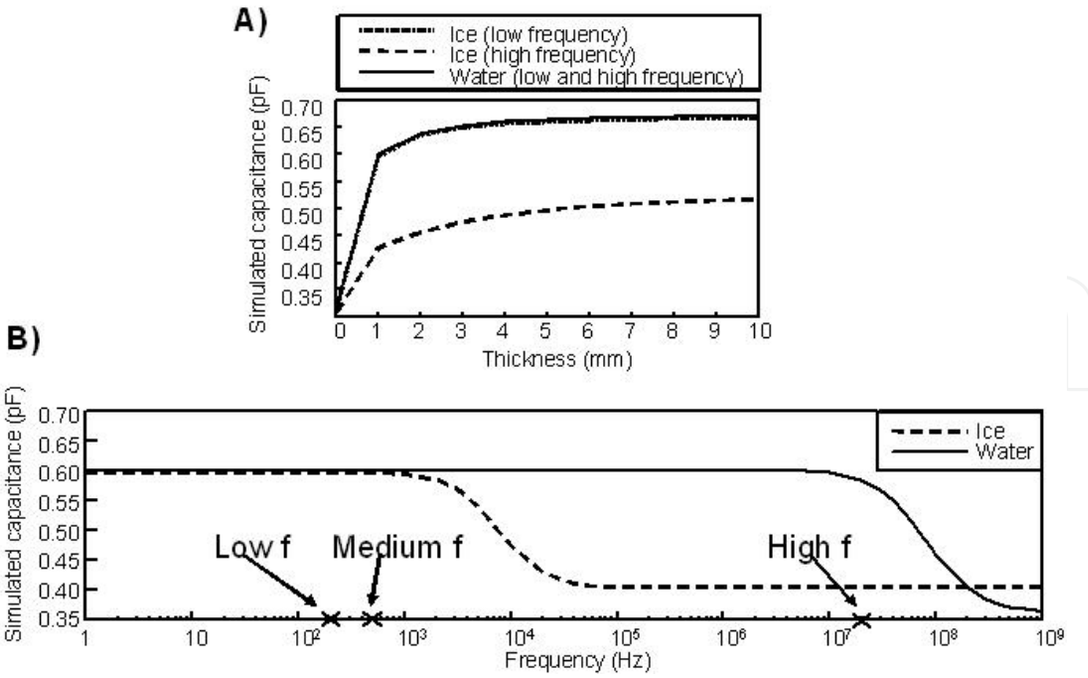

Figure 10. Simulation tests result. A) Simulated capacitance values at different thickness of water and ice (temperature of 25°CC for water and -10°CC for ice). B) Simulated capacitance values at different measurement frequencies when water and ice were placed over the sensor (thickness of 1 mm, and temperature of 25°CC for water and -10°CC for ice).

the road core, and evaluating the dispersion of the time instants in which phase changes were detected. Experimental tests were executed inserting the sensors and the road core in the climatic chamber. At the top of the climatic chamber, an USB webcam (Logitech - QuickCam Pro 9000; operative temperature range from -20°C to +60°C) was inserted to acquire images from the road core in order to detect the formation of the ice over it. A PC was used to store images from the USB webcam and sensory data from the sensors. Images and data were simultaneously acquired using a sampling frequency of 1 sample per minute.

Two different experimental tests were performed, the first imposing a linear gradient of temperature, the second leaving the climatic camber in static condition. Specifically, in the first test, the sensors and the road core were first introduced into the climatic chamber with a temperature of 25°C, for approximately 10 minutes in order to wait that the indications of the sensor became stationary. Then, 1 mm of tap water was placed over each sensor and at the center of the road core. Different temperature gradients were applied and the time instants in which the sensors identified ice formation and the road core surface froze were investigated. Specifically, the climatic chamber was arranged to reach -20°C with different temperature gradients equal to -0.25°C/min, -0.5°C/min, and -0.75°C/min. During this period, the water froze. Once reached the minimum temperature of -20°C, the climatic chamber kept stable conditions for approximately 10 minutes, and then it was arranged to reach 25°C with opposite temperature gradient. During this period, the ice melted. The climatic chamber kept the temperature of 25°C for approximately 10 minutes. Then, sensors and the road core were dried. In the second test, sensors and road core were first placed in the climatic chamber. Then, the chamber was arranged to reach -10°C with a temperature gradient of -1°C/min. Once reached the temperature of -10°C, the climatic chamber was arranged to keep stable conditions. One mm of tap water was placed over each sensor and at the center of

the road core. After closing the chamber, the water placed over the sensors and the road core froze. Then, the climatic chamber was open at ambient conditions and the ice melted. Finally, sensors and the road core were dried. This experiment was repeated in three different days in order to investigate the repeatability of the data.

The results of the experiments are shown in Figure 11. The time intants of formation and melting of ice are shown for the sensors and compared to those in which the same happened over the road model. There was always a negative bias between the indication of the sensors and the conditions of the road. It is worth noticing that there is a deviation between the indications of the sensor and what happens over the road core, as the indications of the sensor anticipate the road conditions. Ice forms before over the sensor, due to the smooth surface of the sensor, which facilitates the formation of ice crystals on it than over the road. Moreover, ice melts before over the sensor than over the road core: this is probably due to the low power consumption of the electronics, which warms the surface of the sensor.

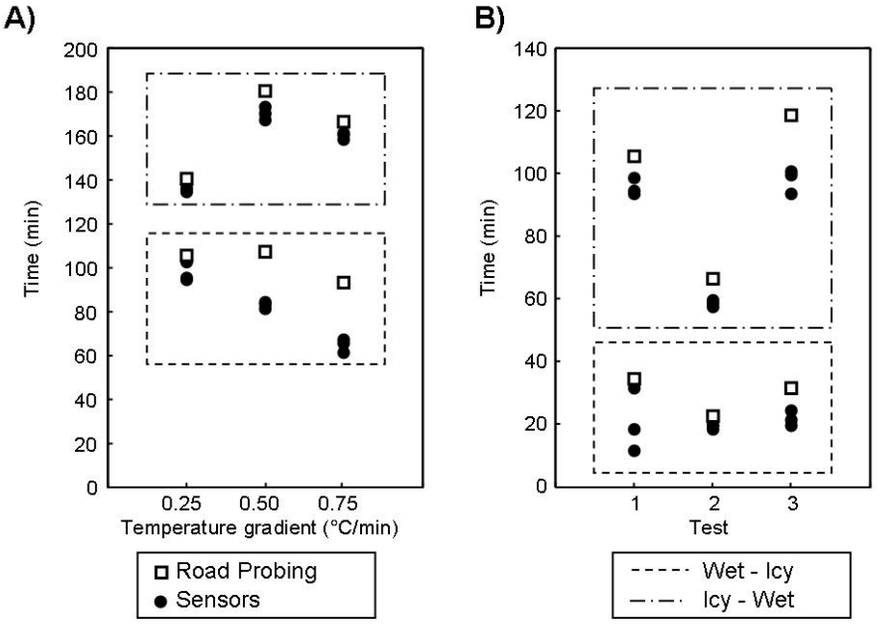

Figure 11. Time instants in which ice formed or melted over the road core compared to the indications of the sensors. A) First experiments, in which different gradients of temperature are applied. B) Second experiments, in which stable conditions at -10°C were maintained by the chamber till water froze and then it was switch off and the door was opened.

5.4. Effect of salt in the water

As one of the main problems in taking measures is the presence of salt spread over the road to avoid ice formation, the output of the sensor when covered by a ionic solution is investigated considering both a simulation model and experiments in the laboratory.

Simulations were performed using a mathematical model of the sensor which extends the one descript above. The model includes the electrode assembly and three planar layers over it, describing Arnite, a ionic solution (modelling a solution of water and salt), and air. Potential satisfies Laplace equation in the Arnite and in air (as no ion is present there) and Poisson

equation in the ionic solution, where the ions contribute as a source term. Ions are present only in the ionic solution and satisfy continuity equation, which accounts for their diffusion and transport within the electric field generated by the external potential. The equations considered for each layer are the followings:

$$\begin{cases} \Delta\phi_1 = 0 \\ \Delta\phi_2 = -\frac{q}{\varepsilon} \cdot (n_+ - n_-) \\ \frac{\partial n_\pm}{\partial t} = D_\pm \cdot (\Delta n_\pm \pm \frac{q}{kT} n_\pm \Delta\phi_2) - D_\pm \cdot (\Delta n_\pm \pm \frac{q}{kT} N \Delta\phi_2) \\ \Delta\phi_3 = 0 \end{cases} \tag{13}$$

where q is the electrical charge of the ions, k is the Boltzman constant, T is the absolute temperature, $n_\pm$ indicates the positive or negative ion densities, $D_\pm$ is their diffusion coefficient (Na^+: $1.33 \cdot 10^{-9} m^2 s^{-1}$; Cl^-: $2.03 \cdot 10^{-9} m^2 s^{-1}$), and N is the density of the ions in thermodynamic equilibrium. The analysis is performed in the limit of small amplitude of the applied voltage (with respect to the thermal voltage), so that the response of the sample to the external signal is linear (the ion densities can be approximated with their value at equilibrium in the continuity equations) [2]. For the ions, the boundary condition was that the current density flowing across the boundary of the second layer (in which they are located) was zero. Experiments were also performed in the laboratory to assess the effect of dissolving different quantities of salt in the water covering the surface of the sensor. The values of capacitance at both high and low frequencies were acquired for one sensor covered by 2ml of water with different concentrations of salt, with salinity between 20% and 100%. The maximum value of salinity (100%) was obtained dissolving 36mg of salt per 100ml of water [10].

The impedance of the sensor at different concentrations of salt dissolved into the water is shown in Figure 12, for both simulations and experiments in the laboratory. Different percentages of salinity (from 20% to 100%) were considered. In the case of the experiments, for each salinity value, data were acquired for five minutes and mean and standard deviation of the measured capacitance were computed. Also data for pure water (without adding salt) are shown. Simulations indicated that the presence of ions in the water reduces the electrical resistance measured by the sensor monotonically with the increase of the concentration of the ions. Nevertheless, the imaginary part of the impedance is much larger than the real one for the two operating frequencies considered, so that the system is essentially insensitive to the presence of salt in the solution, as also indicated by the experiments.

5.5. Experiment in the field

Behavior and robustness of the sensors were studied in the field. Three sensors were embedded at the Turin-Caselle airport in order to detect formation of ice at the beginning, ending and in the middle of the runway, and increase safety during take off and landing of the aircrafts. Moreover, a complete weather station (PCE Group - PCE FWS-20) was placed close to the sensors to monitor meteorological variables, such as ambient humidity, temperature, pressure, velocity and direction of the wind, and quantity of rain falls. On field experiment lasted for a 36 days period (12/01/2010 - 17/02/2010).

Values of capacitance obtained by one of the three sensors (high and low measurement frequencies) during the in the field experiment are shown in Figure 13. In detail, capacitance

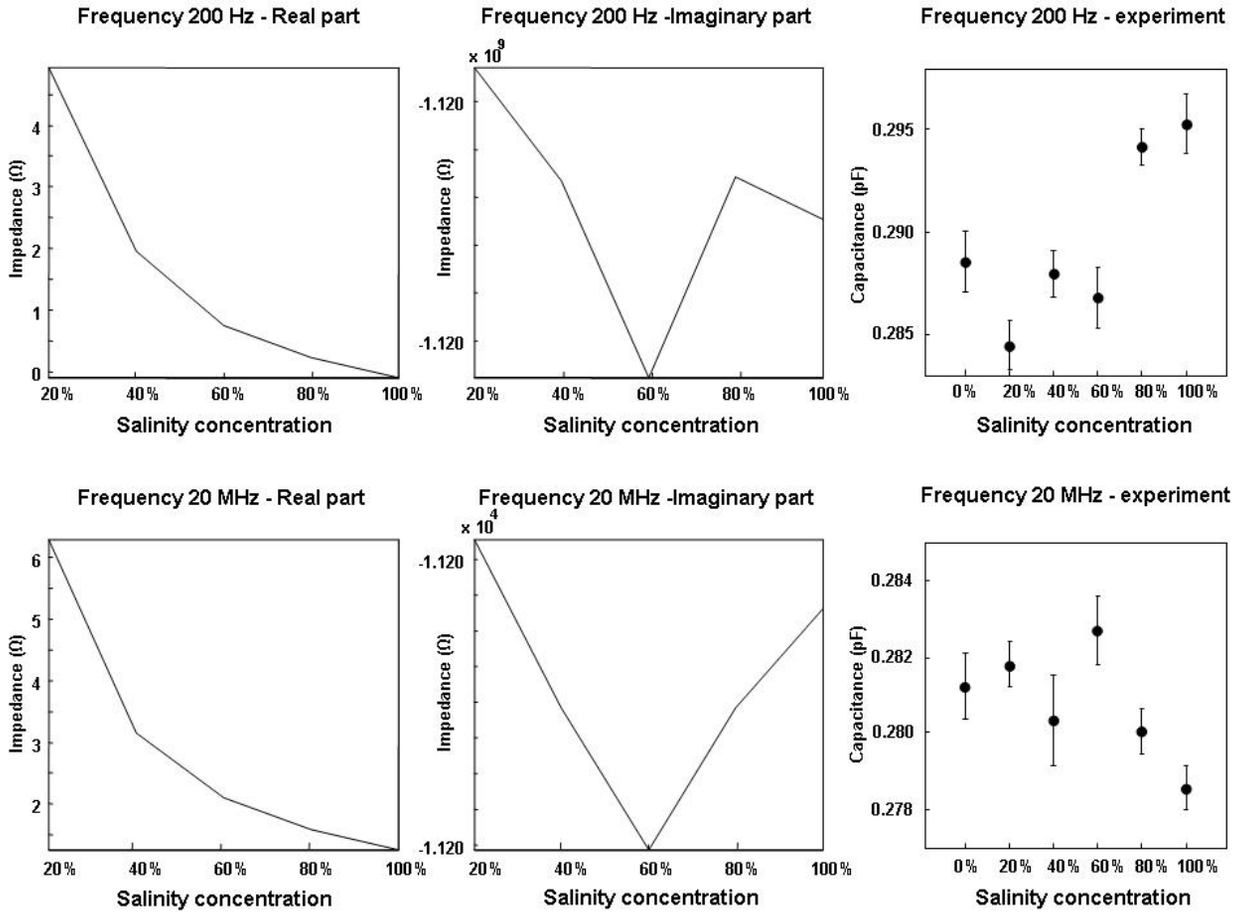

Figure 12. Impedance and capacitance of the system with different salinity, obtained in simulation (layer of water solution 5mm thick) and with experiments (2ml of solution were put over the sensor surface).

values (raw data) at low and high measurement frequencies are shown in Figure 13A. Variations of the values of capacitance over a 36 days period are clearly visible, since the state of the sensor (dry, wet, or icy) continuously changed. States of the standard sensor revealed by the algorithm are shown in Figure 13B. The algorithm was validated during the laboratory tests, so the states revealed for each sensor during the on field test were assumed correct. Environmental data obtained by the weather station are shown in Figure 13C (quantity of rain falls), Figure 13D (humidity of the air), and Figure 13E (temperature of the air). Environmental data are used to examine the correct estimation of the state of the sensor.

During the test period, the sensors revealed different road surface conditions (dry, wet, and icy). Wet condition of the surface of the runway was identified also in the case of fog, confirming that even a slow condensation of water over the sensor surface is associated to a jump in the value of capacitance that may be easily identified Transition to icy conditions were identified when the sensor was wet and temperature decreased to a negative value.

5.6. Relation between sensor output and weather conditions

Considerations about the correlation between weather data and state of the surface of the sensor are studied, with special attention to the weather data during ice formation and the relation between relative humidity and variation of the measured capacitance of the sensor.

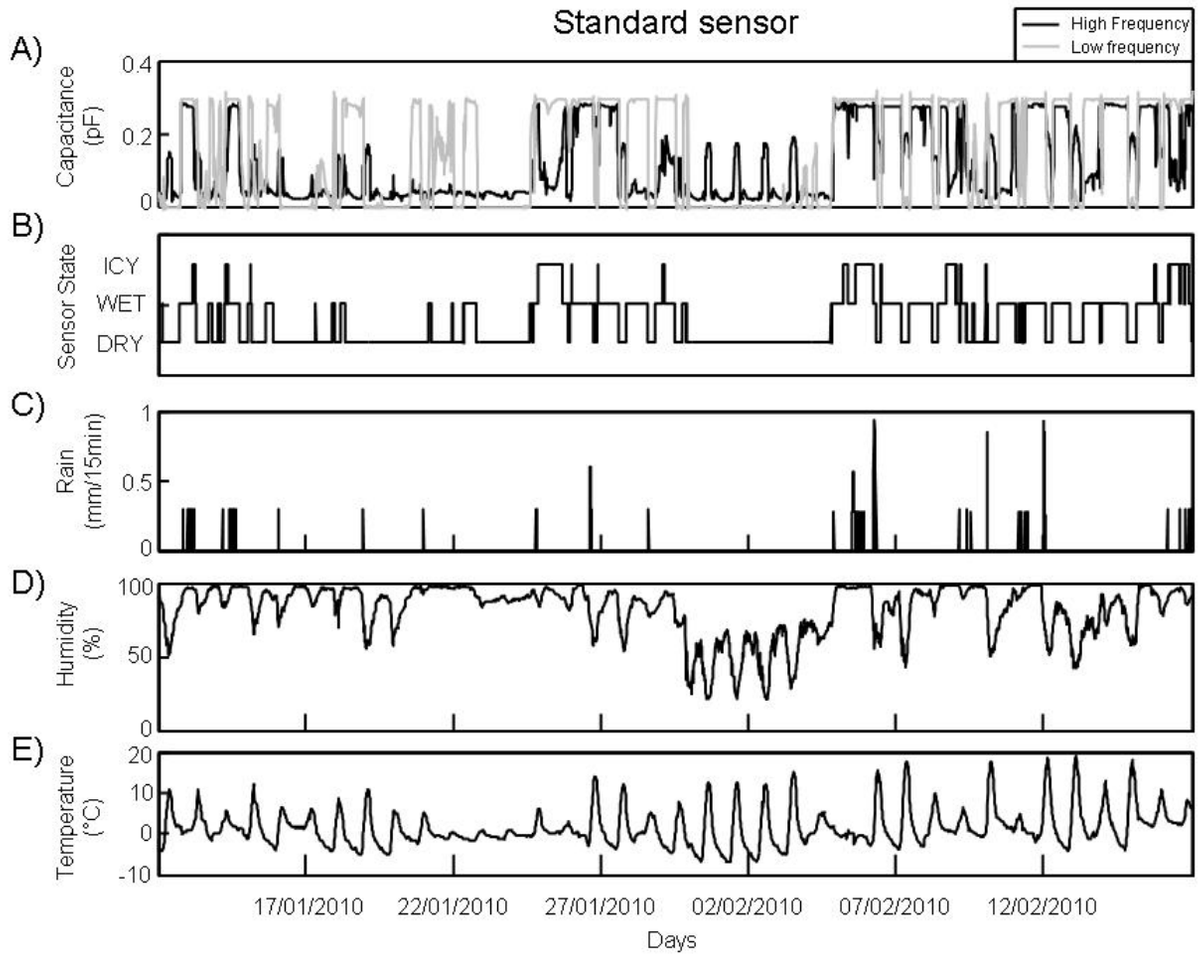

Figure 13. On field results obtained from a sensor placed at the Turin-Caselle airport over the period 12/01/2010 - 17/02/2010. A) Values of capacitance (raw data) obtained for the sensor. B) States of the sensors revealed by the algorithm. C) Quantity of rain falls. D) Ambient humidity. E) Ambient temperature.

Capacitance values from the sensors embedded at the airport were used. Weather conditions in airports are usually reported in the form of a METAR (METeorological Aerodrome Report), which is a format for the transmission of weather data (temperature, dew point, humidity, pressure, wind velocity and direction, quantity of rain falls, and solar radiation) together with considerations about the observed weather condition (sun, cloud cover, rain, snow, etc.). METAR data are on-line available for nearly every airport in the world. Reports are generated about twice an hour (sampling period is usually 30 minutes, but sometimes a pair of data is sampled with 10 minutes delay). The Turin airport is coded as LIMF in the METAR database. Data from January 2010 to September 2010 were used for the comparison with the indication provided by the sensors.

Data were first interpolated in order to be defined on the same time samples, with period of 1 minute. Data from the ice sensors and weather data were linearly interpolated. The observed weather conditions given by the METAR database were interpolated with a nearest neighbour approach. Correlation was estimated between the state provided by each sensor and the information of the observed weather condition provided by the METAR system. The observed

weather conditions were grouped in 4 classes, indicating rain, fog, snowfall and none of the above. The first three observations were correlated with the wet state provided by the sensors. Since the road remains wet also after rain, fog or snowfall stopped, correlation was estimated only within periods in which the METAR indications were rain, fog, or snow, respectively. The icy state provided by the sensors were correlated with the following prediction algorithm: ice forms on the ground if the air temperature is lower than 0°C and the absolute difference between air temperature and the dew point is lower or equal to 1°C [1]. The dew point T_D , that is the temperature to which air must be cooled to trigger condensation of its water vapour, was estimated as [14]:

$$T_D = T - 31.25[2 - log(RH)] \tag{14}$$

where T is the air temperature in Celsius and RH the relative humidity. The values of air temperature and relative humidity were also provided by the METAR system. This algorithm indicates that the region of parameters T and RH allowing the formation of ice is the following:

$$\begin{cases} T < 0 \\ RH > 93\% \end{cases} \tag{15}$$

The correlation between the wet state estimated by the sensors and the rain indication provided by the present weather sensor of the METAR system is shown in Table 1. Correlation is always upper than 90%, it is higher during winter months with respect to the summer months.

	Sensor A	Sensor B	Sensor C
January	100.0%	100.0%	100.0%
February	96.0%	93.6%	100.0%
March	99.0%	97.9%	97.9%
April	100.0%	100.0%	98.1%
May	96.0%	95.6%	91.7%
June	94.6%	93.0%	92.6%
July	90.8%	93.4%	95.2%
August	94.7%	91.6%	93.1%

Table 1. Correlation between the wet state provided by the sensors and the rain indication provided by the METAR system.

The fog indication was obtained by the present weather sensor of the METAR system only during winter. Correlation between the wet state provided by the sensors and the fog indication of the METAR system is shown in Table 2. Correlation is higher than 51% in January and higher than 85% during February and March.

	Sensor A	Sensor B	Sensor C
January	58.9%	54.0%	51.3%
February	91.8%	94.7%	88.5%
March	100.0%	85.7%	96.5%

Table 2. Correlation between the wet state provided by the sensors and the fog indication provided by the METAR system.

Snow fell during the first three months of the year. Correlation between the wet state of the sensors and the snowfall indication provided by the present weather sensor of the METAR

system is shown in Table 3. Correlation is higher than 92% in January and February, and decrease to about 80% in March.

	Sensor A	Sensor B	Sensor C
January	92.6%	100.0%	100.0%
February	99.6%	100.0%	100.0%
March	95.7%	79.2%	92.2%

Table 3. Correlation between the wet state provided by the sensors and the snow indication provided by the METAR system.

The ice indication was obtained by the sensor during the first three months of 2010. Correlation between the icy state provided by the sensors and the ice indication estimated by the prediction algorithm above described is shown in Table 4. Correlation is quite low for all the sensors.

	Sensor A	Sensor B	Sensor C
January	48.5%	64.6%	43.2%
February	78.1%	73.0%	62.2%
March	28.2%	36.1%	39.3%

Table 4. Correlation between the icy state provided by the sensors and approximation that ice can be found on the ground.

Correlation with rain and snowfall was higher than that with fog, which could wet the road only when it lasted a long time. Correlation between the indications of the sensors and of the prediction algorithm was low. This is due to many reasons. For example, in the case in which a thick layer of ice formed over the sensor and started to melt (as correctly predicted by the algorithm) due to the changed weather conditions, the sensor would still indicate that its surface is frozen, until the complete melting of the layer of ice. It should also be considered that the sensor surface could be wet after raining, even if the relative humidity measured by a weather station is lower than that required by the algorithm to predict the formation of ice: in such a condition, it is sufficient that the temperature lowers under 0°C to get ice over the sensor, regardless the value of the relative humidity. Moreover, the formation of ice depends on the concentration of the water covering the surface of the sensor, which could be dirty.

6. Conclusions

A low cost capacitive sensor for the estimation of road condition is presented. Performances of the sensor were investigated in simulations, laboratory and in the field experiments. Laboratory results showed that the sensor correctly identified the presence of air, water, or ice on its surface. Repeatability was satisfied, as different sensors provided the same indication with time delay of a few minutes during different laboratory experiments. Simulation results showed that the mathematical model correctly simulates the behavior of the sensor, allowing the simulation of different sensor conditions. Moreover, laboratory and simulation results showed that the sensor is not sensitive to salt present over the its surface. In the field results showed that the sensors placed at the Turin-Caselle airport worked properly, recognizing air, water, or ice over the runway. Finally, the device provided information consistent with the METAR message for the whole period of study.

The sensor may find applications in monitoring road conditions to support information systems assuring security and efficient maintenance of roads or airports during winter.

However, the descript sensor has a limitation. The measured value of capacitance depends on possible contaminations (e.g. dirt, or fuel) present in the water covering the sensor. Contaminants may change the relative permittivity of the water or ice, or even its variation with frequency, modifying the functionality of the sensor. For this reason, the detection of possible contaminations should be useful, in order to correct the wrong indication of the sensor.

7. Future works

Future works will be focused on the estimation of the thickness of the water or ice placed over the sensor. Since simulations showed that the capacitance values of the sensor increase with the increasing of the thickness of the water or ice placed over the sensor, the sensor can be also used for the estimation of this information. The estimation of the thickness of water can be useful to quantify, for example, the quantity of rain falls.

Nevertheless, the precision of the estimates of the sensor indicates its feasibility for different applications, such as ice forecasting using an artificial neural network, also using the local weather data available.

Finally, future works will be focused on the detection of the presence of snow or frost on the road and runway surfaces. At present, the sensor detects both snow and frost as water, but should be possible to distinguish between them. Moreover, the discrimination between different types of liquid solutions should be possible using the sensor.

Acknowledgment

This work was sponsored by the national projects AWIS (Airport Winter Information System) and ITACA (Innovazione Tecnologica, Automazione e nuovi Controlli Analitici per migliorare la qualità e la sicurezza dei prodotti alimentari piemontesi), both funded by Piedmont Authority, Italy.

Author details

Amedeo Troiano, Eros Pasero and Luca Mesin
Politecnico di Torino - Dipartimento di Elettronica,
Italy

8. References

[1] Baier, W., Shaw, R., Thompson, L. & Felch, R. [1976]. Agrometeorology of the maize (corn) crop, *Proceedings of Symposium on the Agrometeorology of the Maize (Corn) Crop*, Ames, Iowa, USA.

[2] Barbero, G. & Alexe-Ionescu, A. [2005]. Role of the diffuse layer of the ionic charge on the impedance spectroscopy of a cell of liquid, *Liquid Crystals* 32(7): 943Ű949.

[3] Bassey, C. & Simpson, G. [2006]. A comparison of the coplanar waveguide (cpw) and conductor-backed coplanar waveguide (cbcpw) for use as aircraft ice sensors, *Proceedings of Antennas and Propagation Society International Symposium*, Albuquerque, New Mexico.
[4] Bassey, C. & Simpson, G. [2007]. Aircraft ice detection using time domain reflectometry with coplanar sensors, *Proceedings of IEEE Aerospace Conference*, Big Sky, Montana.
[5] Buchner, R., Barthel, J. & Stauber, J. [1999]. The dielectric relaxation of water between 0°C and 35°C, *Chemical Physics Letters* 306: 57–63.
[6] Ezraty, R. [2003]. New-ice detection using microwave sensors, *Proceedings of International Geoscience and Remote Sensing Symposium (IGARSS)*, Toulouse, France.
[7] Gao, H. & Rose, J. [2009]. Ice detection and classification on an aircraft wing with ultrasonic shear horizontal guided waves, *IEEE Transactions on Ultrasonics, Ferroelectrics and Frequency Control* 56(2): 334–344.
[8] Herique, A. & Kofman, W. [1997]. Determination of the ice dielectric permittivity using the data of the test in antarctica of the ground - penetrating radar for mars '98 mission, *IEEE Transactions on Geoscience and Remote Sensing* 35(5): 1338–1349.
[9] Homola, M., Nicklasson, P. & Sundsbø, P. [2006]. Ice sensors for wind turbines, *Cold Regions Science and Technology* 46(2): 125–131.
[10] Howard, R. & Mendelssohn, I. [1999]. Salinity as a constraint on growth of oligohaline marsh macrophytes ii. salt pulses and recovery potential, *American Journal of Botany* 86(6): 795Ű806.
[11] Huhta, C. & Choquette, Y. [2005]. Ice detection and under-ice flow monitoring using a sontek argonaut-sw, *Proceedings of VIII Working Conference on Current Measurement Technology (IEEE/OES)*, Piscataway, New Jersey.
[12] Ikiades, A., Armstrong, D. & Howard, G. [2007]. Optical diffusion and polarization characteristics of ice accreting in dynamic conditions using a backscattering fibre optic technique, *Sensors and Actuators A: physical* 140(1): 43–50.
[13] Ikiades, A., Howard, G., Armstrong, D. J., Konstantaki, M. & Crossley, S. [2007]. Measurement of optical diffusion properties of ice for direct detection ice accretion sensors, *Sensors and Actuators A: physical* 140(1): 24–31.
[14] Iribarne, J. & Godson, W. [1981]. *Atmospheric thermodynamics*, Springer Science & Business.
[15] Jackson, J. [1998]. *Classical Electrodynamics*, Wiley.
[16] Jose, K., Sunil, G., Varadan, V. & Varadan, V. [2002]. Wireless idt ice sensor, *Proceedings of International Microwave Symposium*, Seattle, Washington.
[17] Kawano, K. & Kudoh, J. [2003]. Four-dimensional histogram method for sea ice detection using noaa avhrr images, *Proceedings of International Geoscience and Remote Sensing Symposium (IGARSS)*, Toulouse, France.
[18] Lee, N., Karimi, H. & Krakiwsky, E. [1989]. Road information systems: Impact of geographic information systems technology to automatic vehicle navigation and guidance, *Proceedings of Vehicle Navigation and Information Systems Conference*, Toronto, Canada.
[19] LeVeque, R. [2007]. *Finite Difference Methods for Ordinary and Partial Differential Equations*, Society for Industrial and Applied Mathematics (SIAM).
[20] Li, W., Zhang, J., Ye, L. & Zhang, H. [2009a]. Fiber-optic ice detection system for aeroplane application, *Proceedings of International Workshop on Intelligent Systems and Applications*, Wuhan, China.

[21] Li, W., Zhang, J., Ye, L. & Zhang, H. [2009b]. A fiber-optic solution to aircraft icing detection and measurement problem, *Proceedings of International Conference on Information Technology and Computer Science*, Kiev, Ukraine.
[22] Liu, Y., Keyb, J., Freya, R., Ackermana, S. & Menzel, W. [2004]. Nighttime polar cloud detection with MODIS, *Remote Sensing of Environment* 92(2): 181–194.
[23] Meindl, T., Moniaci, W., Pasero, E. & Riccardi, M. [2006]. An embedded hardware-software system to detect and foresee road ice formation, *Proceedings of IJCNN 2006*, Vancouver, Canada.
[24] Meissner, T. & Wentz, F. [2004]. The complex dielectric constant of pure and sea water from microwave satellite observations, *IEEE Transactions on Geoscience and Remote Sensing* 42(9): 1836–1849.
[25] Mesin, L., Troiano, A. & Pasero, E. [2010]. In field application of an innovative sensor for monitoring road and runway surfaces, *Proceedings of SENSORDEVICES 2010*, Venice, Italy.
[26] Muramoto, K., Saitoand, H., Matsuura, K. & Yamanouchi, T. [1997]. Cloud and ice detection using noaa/avhrr data, *Proceedings of International Geoscience and Remote Sensing Symposium (IGARSS)*, Singapore, Singapore.
[27] Pasero, E., Moniaci, W. & Raimondo, G. [2008]. Awis: an airport winter information system, *Proceedings of SIRWEC 2008*, Prague, Czech Republic.
[28] Petrenko, V. & Whitworth, R. [1999]. *Physics of ice*, Oxford University Press Inc.
[29] Roy, S., DeAnna, R., Izad, A. & Mehregany, M. [1998]. Miniature ice detection sensor systems for aerospace applications, *Proceedings of XI International Workshop on Micro Electro Mechanical Systems (MEMS)*, Heidelberg, Germany.
[30] Roy, S., Izad, A., DeAnna, R. & Mehregany, M. [1998]. Smart ice detection systems based on resonant piezoelectric transducers, *Sensors and Actuators A: phisical* 69: 243–250.
[31] Skolunov, A. [1997]. Frequency-temperature curve of the complex dielectric constant and refractive index of water, *Fibre Chemistry* 29(6): 367–373.
[32] Topp, G., Yanuka, M., Zebchuk, W. & Zegelin, S. [1988]. Determination of electrical conductivity using time domain reflectometry: Soil and water experiments in coaxial lines, *Water Resources Research* 24(7): 945–952.
[33] Troiano, A., Pasero, E. & Mesin, L. [2010]. An innovative water and ice detection system for road and runway surfaces monitoring, *Proceedings of PRIME 2010*, Berlin, Germany.
[34] Troiano, A., Pasero, E. & Mesin, L. [2011a]. Detection of ice formation over a road surface, *Proceedings of SENSORDEVICES 2011*, Nice, French.
[35] Troiano, A., Pasero, E. & Mesin, L. [2011b]. In the field application of a new sensor for monitoring road and runway surfaces, *Sensors & Transducers* 10: 71–83.
[36] Troiano, A., Pasero, E. & Mesin, L. [2011c]. New system for detecting road ice formation, *IEEE Transactions on Instrumentation and Measurement* 60(3): 1091–1101.
[37] Vivekanandam, J., Martner, B. & Politovich, M. [1998]. Aircraft icing detection using dual-wavelength and polarizationradar observations, *Proceedings of International Geoscience and Remote Sensing Symposium (IGARSS)*, Seattle, Washington.
[38] Von Hippel, A. [1988]. The dielectric relaxation spectra of water, ice, and aqueous solutions, and their interpretation. critical survey of the status-quo for water, *IEEE Transaction on Electrical Insulation* 23(5): 801–840.
[39] Wang, M. & Shi, W. [2009]. Detection of ice and mixed ice-water pixels for modis ocean color data processing, *IEEE Transactions on Geoscience and Remote Sensing* 47(8): 2510–2518.